

## Supplementary Information

# **Nanoconfinement of redox reactions enables rapid zinc iodide energy storage with high efficiency**

*Juhan Lee,<sup>ab</sup> Pattarachai Srimuk,<sup>ab</sup> Simon Fleischmann,<sup>ab</sup>  
Alexander Ridder,<sup>ab</sup> Marco Zeiger,<sup>ab</sup> and Volker Presser<sup>ab\*</sup>*

<sup>a</sup> INM - Leibniz Institute for New Materials, 66123 Saarbrücken, Germany

<sup>b</sup> Department of Materials Science and Engineering, Saarland University, 66123 Saarbrücken, Germany

\* Corresponding author's eMail: [volker.presser@leibniz-inm.de](mailto:volker.presser@leibniz-inm.de)

## Section 1: Material characterizations

Nitrogen sorption isotherms (**Fig. S1a**) recorded at  $-196\text{ }^{\circ}\text{C}$  of ACF-1.1 and YP-80F (AC-1.4) can be classified as type I(b) shape. The isotherms for ACF-0.7 and ACF-0.8 are type I(a) implying that ACF-0.7 and ACF-0.8 have narrower pores ( $<1\text{ nm}$ ) than ACF-1.1 and AC-1.4. The pore size distribution (PSD) patterns of AC and ACF were calculated with quenched-solid density functional theory (QSDFT) assuming slit pores. For multi-walled carbon nanotubes (MWCNTs), we applied non-local functional theory (NLDFT) with a hybrid model of slit and spherical pores because this yielded the best fit for the measured data. As can be seen from **Fig. S1b**, all three ACF samples are predominately microporous, whereas AC-1.4 also shows a small mesopore volume, and multi-walled carbon nanotubes (MWCNTs) are exclusively mesoporous. The pore structure parameters (surface area / pore volume / average pore size) can be found in the main manuscript (**Table 1**).

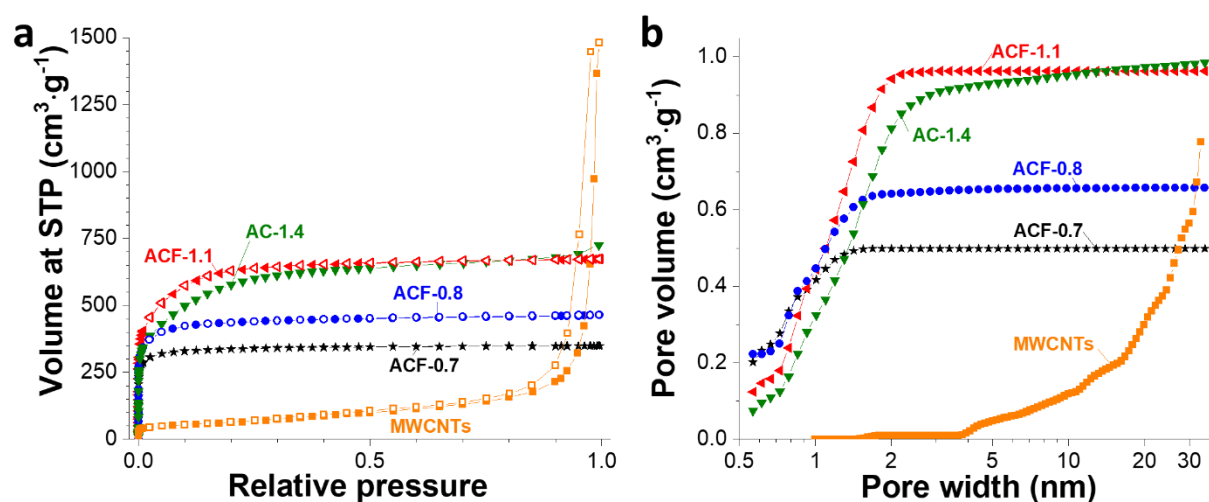


**Fig. S1:** Nitrogen gas sorption analysis of the carbon electrodes applied for this work. a) Nitrogen gas sorption isotherms at  $-196\text{ }^{\circ}\text{C}$ . b) Cumulative pore size distribution per volume.

The morphology of the carbon electrodes was examined by a JEOL JSM 7500F field emission scanning microscope (FE-SEM) at 3 kV (**Fig. S2**). The chemical composition of the carbon electrodes was determined by energy dispersive X-ray spectroscopy (EDX) with an X-Max-150 detector (Oxford Instruments) attached to the SEM chamber (**Table S1**). The spectra of ten spots were measured using an accelerating voltage of 10 kV and averaged; for the calibration, silicon crystal was applied. ACF samples show a highly-intertwined network of porous carbon fibers with an average diameter of about 5  $\mu\text{m}$  and a length of up to several centimeters. The fibers themselves show a high internal porosity, as seen on the fiber surfaces and fracture cross-sections (**Fig. S2a-c**). MWCNT electrodes also form an intertwined network (**Fig. S2d**), whereas the tubes themselves show no internal porosity, as evidenced by GSA. Activated carbon of type AC-1.4 consists of particles in the size of several microns, which are connected by PTFE fibers (**Fig. S2e**). These particles show large, visible pores of up to 1  $\mu\text{m}$  on the surface, which lead to a hierarchical, interparticle pore network.

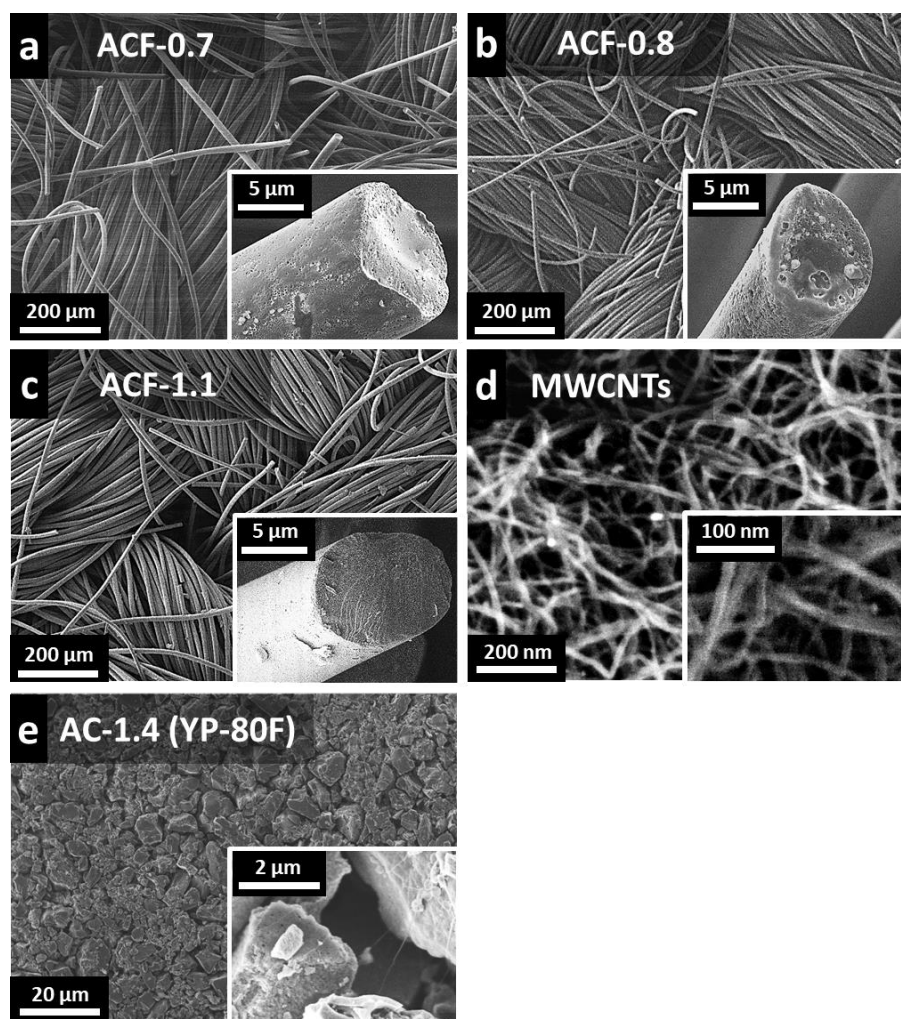


**Fig. S2:** Scanning electron micrographs of the different carbon electrode materials.

**Table S1:** Chemical composition of the carbon electrodes determined by EDX.

Sample	C (mass%)	O (mass%)	Al, F, Na, K, Si (mass%)
MWCNTs	>91	4-6	<4
ACF-0.7	>95	2-4	<1
ACF-0.8	>95	2-4	<1
ACF-1.1	>98	<2	<1
AC-1.4	>95	4-5	<1

Raman spectroscopy was carried out with a Renishaw inVia Raman microscope applying an Nd:YAG laser (532 nm) with a power of ca. 0.25 mW. With a grating of 2400 lines·mm<sup>-1</sup>, yielding a spectral resolution of approximately 1.2 cm<sup>-1</sup>. The spot size on the sample was about 2 μm with a numeric aperture of 0.9. Spectra were recorded for various carbon electrodes with an acquisition time of 30 s and 10 accumulations. D- and G-band deconvolution was carried out with baseline-subtracted, D-band normalized Raman spectra, employing four Voigt peaks.<sup>1</sup> The quantitative results are found in **Table S2**, Raman spectra are given in **Fig. S3**.

Peak deconvolution reveals a decreasing I<sub>D</sub>/I<sub>G</sub> ratio of 2.86, 2.79, and 2.61 for ACF-0.7, ACF-0.8, and ACF-1.1, respectively. Similarly, the FWHM values for the D-signal drop in the same order for these samples, from 141 to 109 cm<sup>-1</sup>. Both a higher I<sub>D</sub>/I<sub>G</sub> ratio, as well as a higher FWHM of the D-signal are generally associated with an increase in structural carbon disorder that is linked to defects in the hexagonal graphite structure.<sup>2</sup> These defects originate mainly from micropores that disrupt the graphitic carbon lattice. The smallest micropores are found in ACF-0.7, causing quantitatively more carbon defects per volume of material, which leads to the highest I<sub>D</sub>/I<sub>G</sub> ratio and D-signal FWHM of this sample. AC-1.4, which exhibits a porosity comparable to ACF-1.1, leading to the same I<sub>D</sub>/I<sub>G</sub> of 2.61, the lower FWHM of the D-signal can be associated with a slightly lower fraction of micropores below 1 nm (**Fig. S1b**). MWCNTs have virtually no intraparticle pores, defects in the graphitic structure are mainly related to vacancies or non-hexagonal carbon rings.<sup>3</sup> Therefore, they exhibit a less defective graphite structure, which leads to by far the lowest I<sub>D</sub>/I<sub>G</sub> (2.06) and FWHM of the D-signal (64 cm<sup>-1</sup>).

**Table S2:** Results of Raman D- and G-band deconvolution Position and full width at half maximum (FWHM) are given, as well as the areal intensity ratio.

Sample	D-mode		G-mode		$I_D/I_G$ ratio
	Position (cm <sup>-1</sup> )	FWHM (cm <sup>-1</sup> )	Position (cm <sup>-1</sup> )	FWHM (cm <sup>-1</sup> )	
MWCNTs	1353	64	1600	67	2.06
ACF-0.7	1337	141	1604	54	2.86
ACF-0.8	1338	126	1604	53	2.79
ACF-1.1	1335	109	1604	49	2.61
AC-0.8	1337	96	1602	55	2.61

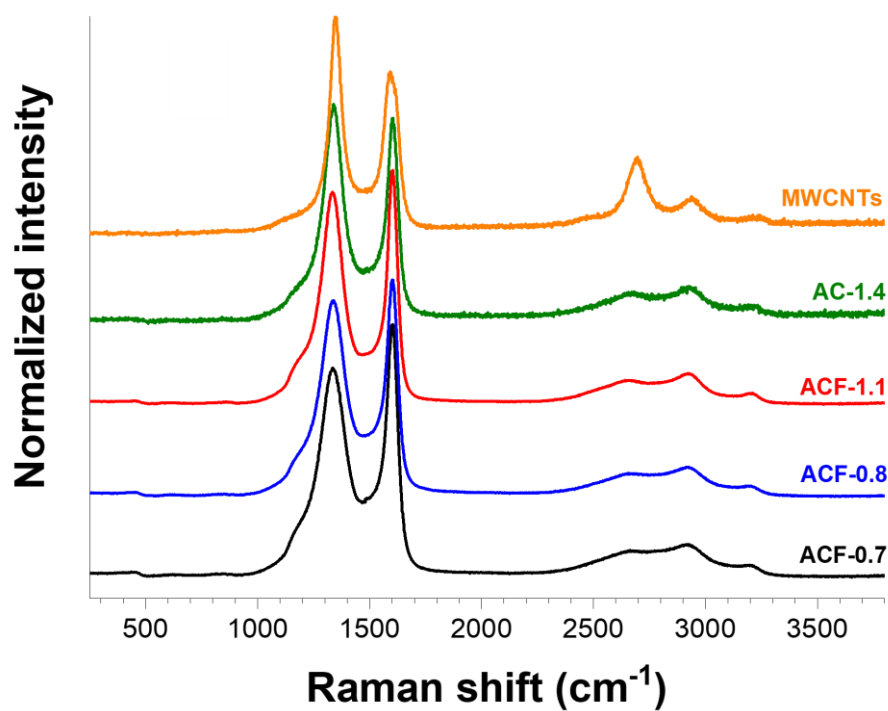


**Fig. S3:** Raman spectra of samples ACF-0.7, ACF-0.8, ACF-1.1, AC-1.4, and MWCNT.

## Section 2: Redox kinetics of potassium ferricyanide and iodide in nanoporous carbon

To investigate the kinetic of redox electrolyte in nanoporous carbon electrodes, we first benchmarked a well-established standard redox couple with one electron transfer, namely 1 M of potassium ferricyanide, PFC. The inset in **Fig. S4a** illustrates cyclic voltammograms of a flat surface electrode (5 mm diameter glassy carbon, GC, ALS GmbH) and nanoporous activated carbon (AC-1.4) coated on GC at a scan rate of  $100 \text{ mV}\cdot\text{s}^{-1}$ . The detailed preparation of the carbon coated GC can be found in Ref.<sup>4</sup>. The CVs of GC and AC-1.4 electrodes exhibit half-wave potential of +0.26 V and +0.21 V vs. Ag/AgCl, respectively, with different oxidation and reduction current response. The reduction currents of GC and AC-1.4 electrodes versus scan rate follow a power law ( $y=ax^e+b$ ) with an exponent of 0.3 for GC and 1.0 for AC-1.4 (**Fig. S4a**). Therefore, the redox kinetics in AC-1.4 electrode seems to follow the recently suggested thin layer diffusion electrochemistry (exponent close to 1) than the planar diffusion electrochemistry (exponent close to 0.5).<sup>5-7</sup>

So far, the thin layer diffusion electrochemistry has been studied mostly with the carbon nanotubes with various arrangement for different type of pore space between the tubes. After the pioneering modeling and simulation work for the thin layer electrochemistry,<sup>5-7</sup> enhanced redox kinetics in porous carbon electrode were reported in case of macroporous and mesoporous carbons via diffusion-less redox reactions and fast ion diffusion in the confined carbon pores, respectively.<sup>8,9</sup> Our results of microporous activated carbon electrode (AC-1.4) strongly support the electrochemical thin layer process from previous reported meso- and macroporous carbon studies. However, since the contribution of electric double-layer (EDL) formation is reported to be significant for high surface carbon electrode in case ferricyanide/ferrocyanide redox couple,<sup>10</sup> the conventional electrochemical analyses could be misleading when the influence of ELD is not considered. Therefore, the influence of the electric double-layer must be excluded for the analysis. The implementation of rotating disk electrode (RDE, RRDE-3A, ALS GmbH) allows us to investigate the redox kinetic in nanoporous carbon since the contribution of electric double-layer can be kept at a constant scan rate while kinetic condition is varied via rotational speed of the electrode.

The bulk hydrodynamic diffusion generated via the spinning of the electrode leads to a thin and constant diffusion layer. Hence, the rate is limited mostly to the diffusion of redox species near the charges transfer zone. **Fig. S4b-c** shows cyclic voltammograms at 100 mV·s<sup>-1</sup> with different rotational speed. By increasing the rotational speed of electrode from 200 rpm to 3200 rpm, the Fe(CN<sub>6</sub>)<sup>-4</sup> ions in bulk regime are transported faster into the diffusion layer. Therefore, the reduction current is increasing as a function of increasing rotational speed. This phenomenon is explained by Koutecky-Levich equation,<sup>4, 11</sup>

$$\frac{1}{j} = \frac{1}{j_k} + \frac{1}{j_L} = \frac{1}{B} \omega^{-0.5} + \frac{1}{nFKC} \quad (\text{Eq. S1})$$

where,  $j$  is the measured current,  $j_k$  the intrinsic kinetic limit current,  $j_L$  is the mass transfer limit current,  $F$  is Faraday constant,  $C$  is bulk concentration, and  $n$  is number of electron involved in the reaction which is the proportional to the square root of angular velocity ( $\omega$ ) of RDE electrode. The proportionality is defined as  $B$ ,

$$B = 0.62D^{2/3}\nu^{-1/3}nFC \quad (\text{Eq. S2})$$

where,  $\nu$  is the kinematic viscosity of the electrolyte and  $D$  is diffusion coefficient of reactant. We assume  $j_k$  to be constant at certain potential with rate constant ( $k$ ).

As shown in **Fig. S4d**, the linear relation between response current and angular speed is obtained. The slope of the graph ( $B^{-1}$ ) corresponds to the diffusion coefficient. The diffusion coefficient was calculated by using  $\nu = 0.00921 \text{ cm}^2\cdot\text{s}^{-1}$ ,  $n=1$ ,  $F=96485 \text{ mol}^{-1}$ , and  $C=0.001 \text{ mol}\cdot\text{cm}^{-3}$ . In case of nanoconfined redox ions (AC-1.4), the diffusion coefficient of  $2.1\cdot 10^{-7} \text{ cm}^2\cdot\text{s}^{-1}$  was obtained while the diffusion coefficient for GC flat electrode was calculated to be  $1.6\cdot 10^{-7} \text{ cm}^2\cdot\text{s}^{-1}$ . The higher diffusion coefficient of the nanoporous carbon than that of GC flat electrode confirms the redox kinetic is enhanced in nanoporous carbon as enabled by the fast diffusion of redox ions in the confinement of carbon nanopores.

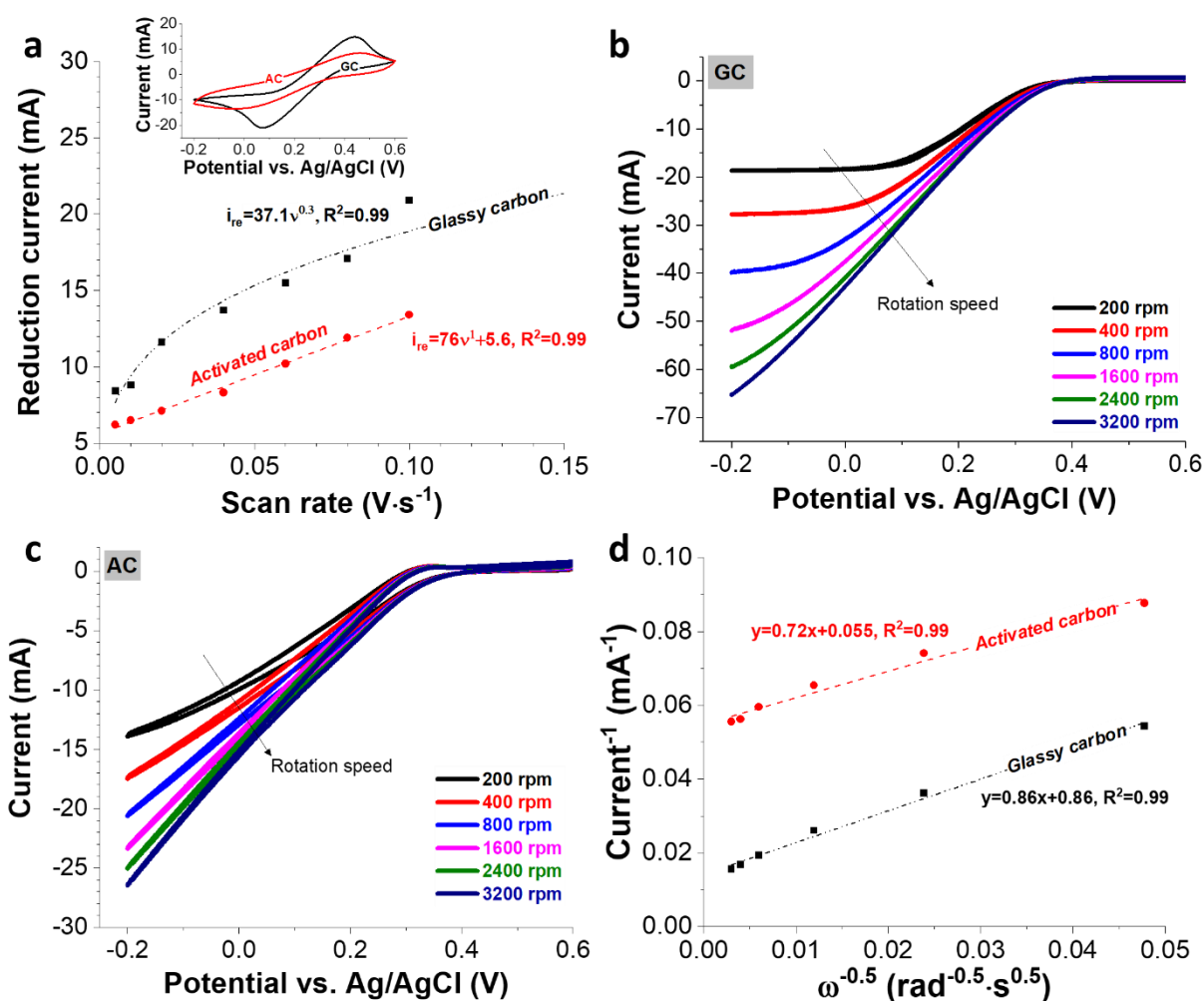


**Fig. S4:** Kinetic study of redox couple (1 M potassium ferricyanide) with cyclic voltammetry under static and dynamic condition. Dynamic condition was given by rotation disk electrode. a) the reduction current versus scan rate corresponding result from cyclic voltammogram (inset) in 1 M potassium ferricyanide, b-c) cyclic voltammogram of GC and AC-1.4 electrode with different rotational speed and d) Koutecky-Levich relation plot.

The same strategy is applied to study kinetic of potassium iodide (KI). Iodide is the complex redox reaction which undergo oxidation by donating two electrons to form iodine/and triiodide at standard potential of 0.54 V vs SHE, afterward the resulting iodine can be reacted with water to form iodate ion at potential of 1.2 V vs SHE. The latter is an irreversible reaction (inset **Fig. S5a**) consuming the iodide ions leading to poor charge efficiency particularly. Therefore, we avoid the second reaction by limiting potential lower than 0.6 V vs. SHE (0.4 V vs. Ag/AgCl):



**Fig. S5a** shows the cyclic voltammograms of AC-1.4 and GC electrode in 0.1 M KI and 0.5 M K<sub>2</sub>SO<sub>4</sub>. In the case of GC, the onset oxidation potential of iodide (I<sup>-</sup>) ion was observed to be at +0.12 V vs. Ag/AgCl. The oxidation current is sharply increase up to 0.15 mA at +0.3 V vs. Ag/AgCl; afterwards, the electrode was backward scanned, leading to reduction of triiodide/iodine(I<sub>2</sub>/I<sub>3</sub><sup>-</sup>). The ratio of oxidation and reduction current (I<sub>re</sub>/I<sub>ox</sub>) is 0.57 suggesting irreversible process possibly due to redox shuttling and precipitation of I<sub>2</sub>.<sup>12, 13</sup> The latter is strongly depended on the identity of electrode such as microstructure and surface chemistry. The cyclic voltammogram of 0.1 M KI and 0.5 M K<sub>2</sub>SO<sub>4</sub> performs differently in AC-1.4 compared to the flat electrode (GC). The onset oxidation potential was observed to be 0.12 V vs. Ag/AgCl, which is 0.18 V lower than in GC electrode possibly via the higher local concentration which trapped inside pores and thin layer diffusion.<sup>8</sup> The I<sub>re</sub>/I<sub>ox</sub> of AC-1.4 is 0.98, confirming that nanoporous carbon mitigate the redox shuttling and favor to form triiodide instead of iodine resulting high degree of reversible reaction. **Fig. S5b** illustrates the reduction current of triiodine on AC-1.4 and GC electrode plotted against the scan rate. By fitting the curve with a power law, the kinetic limit can be identified (**Fig. S5b**): AC-1.4 exhibits an exponent of 0.4 and the GC flat electrode of 0.2. Because the oxidation potential was not scanned till the peak current appears, the low exponent numbers (<0.5) do not necessarily indicate slow redox kinetics in both cases. The reduction current is rather reduced due to the larger peak separation at higher scan rate than the kinetic limitations since the non-equilibrium state of the reaction to the oxidation peak current is growing as the peak separation is getting broader in a fixed potential window for the scanning. Because the thin layer electrochemistry in carbon pores is also featured by the narrow peak separation with less distortion in shape,<sup>5-8</sup> the lower exponent number for AC-1.4 than that of GC flat electrode still implies that the redox kinetics of iodide system in nanopores is faster than on the flat electrode.

Further studies with RDE in 0.1 M KI and 0.5 M K<sub>2</sub>SO<sub>4</sub> (**Fig. S5c**) show that the reduction current for AC-1.4 is slightly increased by increasing of rotating speed being good align with Koutecky-Levich equation (**Fig. S5d**). The slope of curve was 1.26, translating to a diffusion coefficient of  $5.3 \cdot 10^{-3} \text{ cm}^2 \cdot \text{s}^{-1}$ . As compared to a previous study, the diffusion coefficient of I<sup>-</sup> on GC electrode estimated from static condition is between  $1.6 \cdot 10^{-5}$  and  $2.6 \cdot 10^{-7} \text{ cm}^2 \cdot \text{s}^{-1}$  depending on the concentration.<sup>13, 14</sup> These values are much lower than that of AC-1.4 electrode. In addition, the RDE result in GC electrode does not fit to the Koutecky-Levich since we observed no change of reduction and oxidation current when the electrode rotation speed is increased. This is possible when the formation of triiodide ions is dominated by deposition/adsorption of iodine/iodide leading to continuous shuttling process of oxidized triiodide/iodine ion. Since the redox reactions are confined in the case of porous carbons in narrow pores,<sup>8</sup> this active site blocking does not play an influential role in case of AC-1.4. Considering the specific adsorption behavior of iodide,<sup>15</sup> confining iodide into the carbon micropores seems to be crucial for enhanced redox kinetics as well as high reversibility enabled by low-degree of redox shuttling.

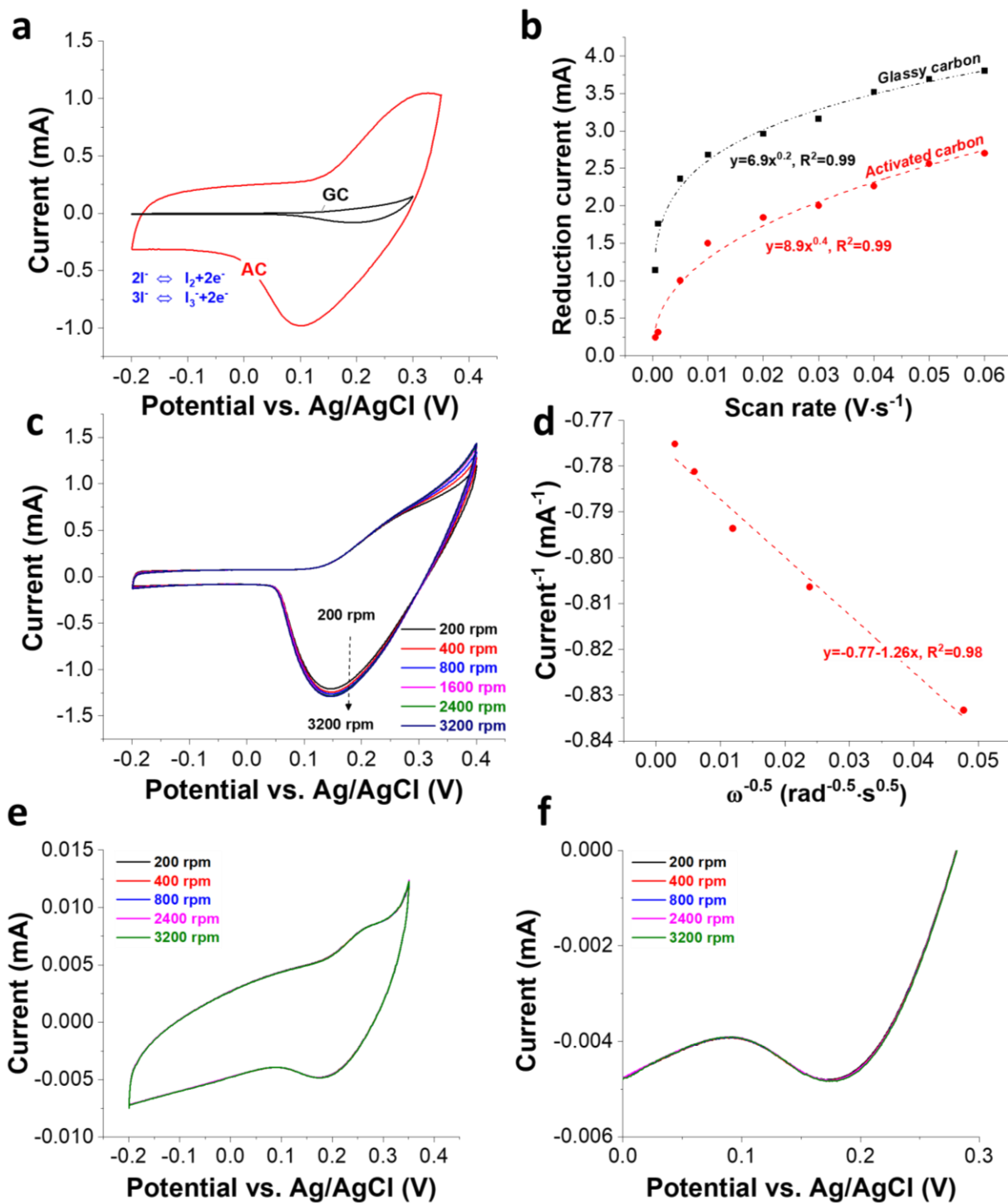


**Fig. S5:** The kinetic study of iodide on GC and AC electrode with cyclic voltammetry under static and dynamic condition. a) Cyclic voltammogram of GC and AC electrode in 0.1 M KI and 0.5 M  $K_2SO_4$ , b) plot of reduction current versus scan rate respecting result from cyclic voltammogram, c) cyclic voltammogram of AC electrode in 0.1 M KI and 0.5 M  $K_2SO_4$  with different rotational speed, d) Koutecky-Levich relation plot, e) and f) cyclic voltammogram of GC electrode in 0.1 M KI and 0.5 M  $K_2SO_4$  with different rotational speed.

### Section 3: Validity of carbon quasi-reference electrode

Porous carbon for use as a quasi-reference electrode has been demonstrated by us in previous work (Ref. <sup>16</sup>). In short, porous carbon can be effectively applied to aqueous electrochemistry when a reproducible reference potential of the applied carbon quasi-reference electrode (QRE) is validated in a certain system with the acceptable stability for the experimental time frame. Considering the scope of our work, the reproducible reference potential within the range of 50 mV is reasonable when the reference potential is stable for at least 48 h; this corresponds with the time required for the characterization of ACF/Zn ZnI<sub>2</sub> batteries and the self-discharge rate of 1 M KI solution with various cathodes in half-cell configuration.

For the determination of the reference potential of the applied carbon QRE (YP-80F with 5 mass% PTFE), activated carbon fiber electrodes (ACF-0.8) were charged to 0.2 mAh at 1.1 mA·cm<sup>-2</sup> in half-cell configuration vs. carbon QRE and the OCP of the ACF-0.8 was measured by subtracting the iR drop (**Fig. S6**, inset). After the OCP period, the cell is discharged until the potential plateau disappeared. By this way, we have ensured that the iodine and triiodide are completely in a reduced state. In this manner, OCPs were measured after various resting time after the cell assembly. We note a small standard deviation of ca. 11 mV from three cells. A particularly stable reference potential can be seen after 30 h which also aligns with our previous observations with potassium ferricyanide containing neutral aqueous solutions.<sup>16</sup> Given that the measured OCP does not shift more than 10 mV for 2.5 d measurement, the applied carbon QRE is considered to be valid for the scope of our work.

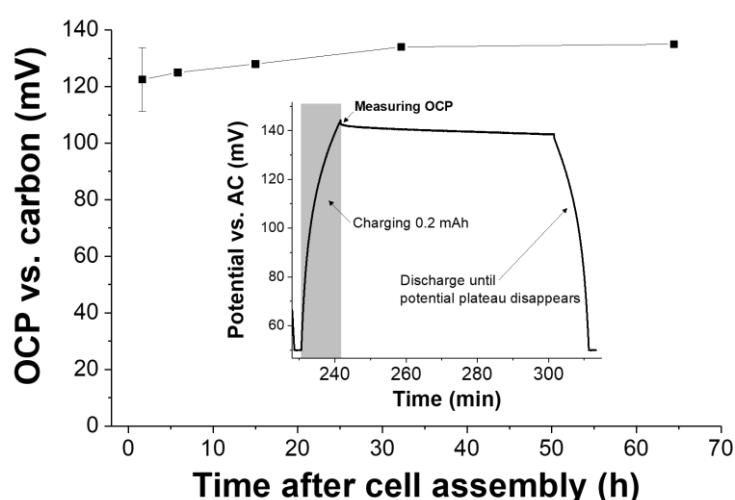


**Fig. S6:** Validity test for porous carbon quasi-reference electrode in 1 M KI solution. The reproducibility and the stability of the reference potential was measured by observing open circuit potential after charging the working electrode up to 1 mAh with the capacity limit of 0.2 mAh.

## Section 4: Stability (S-value) analysis in charge reversibility point of view

Quantitative data analysis of cyclic voltammograms via S-value testing (**Fig. S7**, inset) is an effective analytical method to quantify i) the onset potential window of the chemical decomposition potential or irreversible electrochemical reaction by thorough investigation on the reversibility of the charge,<sup>17, 18</sup> ii) charge storage capacity at the applied voltage window, and iii) cyclic voltammograms containing information about the redox reactions.

The S-value is defined per Ref. <sup>17</sup> as:

$$S = \frac{Q_{char}}{Q_{dis}} - 1 \quad (\text{Eq. S6})$$

where  $Q_{char}$  is the charge accumulated during charging (i.e., oxidation in our case) and  $Q_{dis}$  is the amount of charge released during discharging (i.e., reduction in our case). The comprehensive data from S-value testing can directly be converted in a plot of specific capacity vs. maximum applied cell voltage (**Fig. S7**). The limit for the stable cell voltage can be determined either by the upper S-value limit of 0.1 or by the exponent increase in S-value, which corresponds to irreversible Faradaic reaction.<sup>17, 19</sup> In **Fig. S7**, the maximum stable potential window for ACF-0.8 cathode is determined to be 375 mV (marked gray) where S-value starts increase exponentially. While conducting the S-value analysis, also the potential of the Zn disk was measured (**Fig. S7**). In the stable potential range of the cathode, the Zn disk potential was fluctuating with the amplitude of ca. 0.06 V around 0.97 V implying that the redox potential of  $Zn^{2+}/Zn(s)$  on Zn disk is in that range.

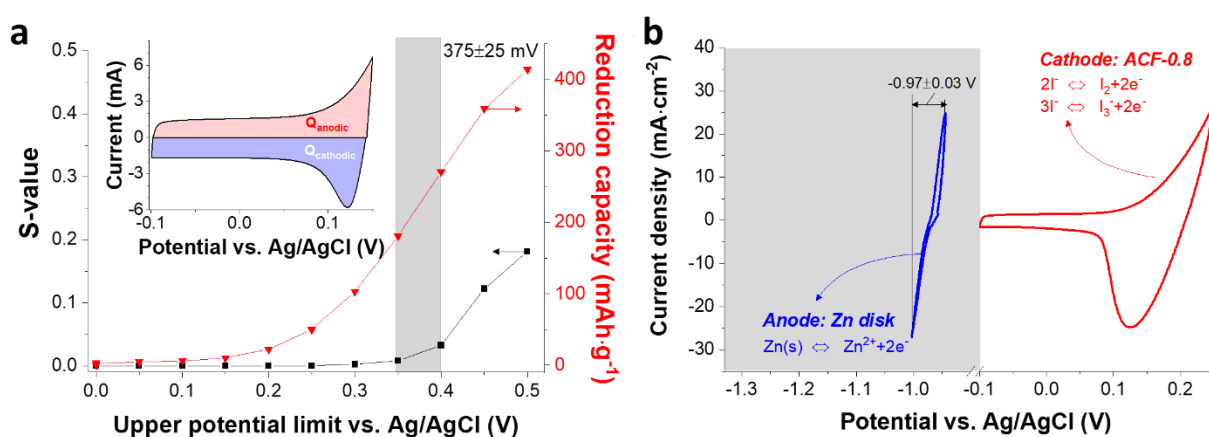


**Fig. S7:** Electrochemical analysis of an ACF/Zn battery in 1.2 M ZnI<sub>2</sub> solution. a) S-value results and reduction capacities are plotted as a function of upper potential limit. Inset shows the cyclic voltammogram obtained as the upper potential limit was set to 0.15 V vs. Ag/AgCl. b) Cyclic voltammograms obtained for ACF-0.8 working electrode as operated by Ag/AgCl reference electrode while recording the potential of the Zn disk counter electrode.

## Section 5: Normalization for Ragone plot

For the evaluation of electrochemical energy storage materials, the most common normalization method is to consider only the mass or volume of the electrode excluding the electrochemically inactive materials such as separators, binder materials, and electrolyte.<sup>20</sup> For the comparison with the other systems, volumetric or gravimetric Ragone charts are often used; however, such comparisons can be misleading since the performance of the commercially available energy storage systems is commonly normalized to the entire cell volume and mass, while the claimed performance is mostly normalized only by the active mass of the electrode.<sup>15</sup> Considering that volume and the mass of the current collectors and the outer housing can be significantly minimized by state of the art engineering techniques, particularly, when the size of the system is getting bigger, normalization to the total mass or volume of the electrode, separator, and electrolyte is a reasonable solution for the comparison to the commercially available systems in Ragone chart. As reported in Ref. 15, a complexity arises for the estimation of the electrolyte mass in porous carbon while volumetric normalization can be easily done by considering the geometrical volume of the electrode, electrolyte, and separator. Following the procedures described in Ref. 15 we calculated the volume of the electrolyte which is filled in the porous carbon via Equation (S7),

$$V_{free} = V_{geo} - \frac{m_c}{\rho_{skel}} \quad (\text{Eq. S7})$$

where  $V_{free}$  is the free volume in the porous carbon filled with electrolyte,  $V_{geo}$  is the geometric volume of the electrode compartment,  $m_c$  is the mass of the activated carbon fiber, and  $\rho_{skel}$  is the skeletal density of the activated carbon electrode which is  $2.1 \text{ g}\cdot\text{cm}^{-3}$ .

For the electrolyte volume in the separators, the following equation is applied.

$$V_{freeS} = V_{geoS} \cdot P_{sep} \quad (\text{Eq. S8})$$

where  $V_{freeS}$  is the free volume in the separator filled with electrolyte,  $V_{geoS}$  is the geometric volume of the separator, and  $P_{sep}$  is the porosity of the separator. For the glassy fiber separator, the porosity was 0.9 and for Celgard 3501 it was 0.55.

Since our volume limited cell does not have space for the electrolyte except the geometric volume of the separator and the electrode, the mass of the total electrolyte ( $m_{el}$ ) in the cell was derived via:

$$m_{el} = (V_{freeS} + V_{free}) \cdot \rho_{el} \quad (\text{Eq. S9})$$

where  $\rho_{el}$  is the measured electrolyte density.

For comparison, the power and energy storage performance are also normalized only by the mass of the electrode (**Fig. S8a**).

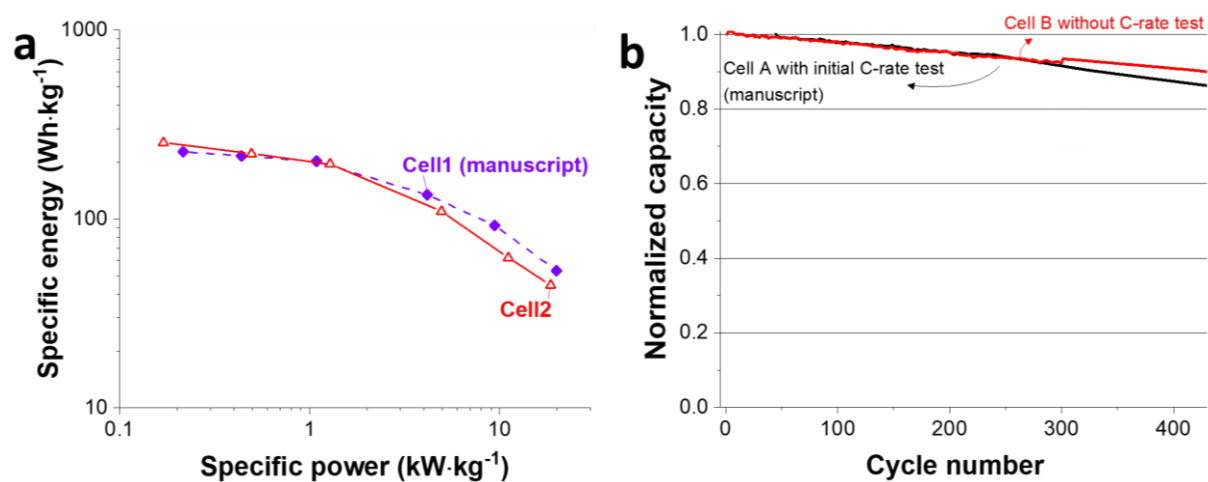


**Fig. S8:** Electrochemical performance of ACF/Zn 1.2 M ZnI<sub>2</sub> battery cells. a) Specific power and energy from two ACF/Zn 1.2 M ZnI<sub>2</sub> battery cells as normalized only by the mass of the electrode. b) Cyclic stability of two ACF/Zn 1.2 M ZnI<sub>2</sub> battery cells. Cell A was characterized with the initial C-rate test while Cell B was characterized without C-rate test. Here, the normalized capacities are shown only from the 1 C-rate results.

## References for Supporting Information

1. M. Zeiger, N. Jäckel, D. Weingarh and V. Presser, *Carbon*, 2015, **94**, 507-517.
2. J. Cebik, J. K. McDonough, F. Peerally, R. Medrano, I. Neitzel, Y. Gogotsi and S. Osswald, *Nanotechnology*, 2013, **24**, 205703.
3. Y. E. Lozovik, S. Ogarkov and A. Sokolik, *Phys. Rev. B*, 2012, **86**, 045429.
4. P. Srimuk, L. Ries, M. Zeiger, S. Fleischmann, N. Jackel, A. Tolosa, B. Krüner, M. Aslan and V. Presser, *RSC Adv.*, 2016, **6**, 106081-106089.
5. K. R. Ward, L. Xiong, N. S. Lawrence, R. S. Hartshorne and R. G. Compton, *J. Electroanal. Chem.*, 2013, **702**, 15-24.
6. M. C. Henstridge, E. J. F. Dickinson, M. Aslanoglu, C. Batchelor-McAuley and R. G. Compton, *Sens. Actuators, B*, 2010, **145**, 417-427.
7. I. Streeter, G. G. Wildgoose, L. Shao and R. G. Compton, *Sens. Actuators, B*, 2008, **133**, 462-466.
8. R. Narayanan and P. R. Bandaru, *J. Electrochem. Soc.*, 2014, **162**, A86-A91.
9. S. Chathoth, E. Mamontov, S. Dai, X. Wang, P. Fulvio and D. Wesolowski, *Europhys. Lett.*, 2012, **97**, 66004.
10. J. Lee, S. Choudhury, D. Weingarh, D. Kim and V. Presser, *ACS Appl Mater Interfaces*, 2016, **8**, 23676-23687.
11. P. Srimuk, M. Zeiger, N. Jäckel, A. Tolosa, B. Krüner, S. Fleischmann, I. Grobelsek, M. Aslan, B. Shvartsev and M. E. Suss, *Electrochim. Acta*, 2017, **224**, 314-328.
12. E. I. Rogers, D. S. Silvester, L. Aldous, C. Hardacre and R. G. Compton, *The Journal of Physical Chemistry C*, 2008, **112**, 6551-6557.
13. C. L. Bentley, A. M. Bond, A. F. Hollenkamp, P. J. Mahon and J. Zhang, *Electrochim. Acta*, 2013, **109**, 554-561.
14. C. L. Bentley, A. M. Bond, A. F. Hollenkamp, P. J. Mahon and J. Zhang, *J. Phys. Chem. C*, 2015, **119**, 22392-22403.
15. S.-E. Chun, B. Evanko, X. Wang, D. Vonlanthen, X. Ji, G. D. Stucky and S. W. Boettcher, *Nat Commun*, 2015, **6**, 7818.
16. J. Lee, N. Jäckel, D. Kim, M. Widmaier, S. Sathyamoorthi, P. Srimuk, C. Kim, S. Fleischmann, M. Zeiger and V. Presser, *Electrochim. Acta*, 2016, **222**, 1800-1805.
17. D. Weingarh, H. Noh, A. Foelske-Schmitz, A. Wokaun and R. Kötz, *Electrochim. Acta*, 2013, **103**, 119-124.
18. J. Lee, D. Weingarh, I. Grobelsek and V. Presser, *Energy Technol.*, 2016, **4**, 75-84.
19. K. Xu, S. P. Ding and T. R. Jow, *J. Electrochem. Soc.*, 1999, **146**, 4172-4178.
20. Y. Gogotsi and P. Simon, *Science*, 2011, **334**, 917-918.